Received: 10 September 2023 | Revised: 15 October 2023 | Accepted: 9 November 2023

DOI: 10.1002/elt2.18

RESEARCH ARTICLE

WILEY

Unveiling the correlation between structural alterations and enhanced high-voltage cyclability in Na-deficient P3-type layered cathode materials via Li incorporation

Xiaoxia Yang[1] | **Suning Wang**[1,2,3] | **Hang Li**[3] | **Jochi Tseng**[4] | **Zhonghua Wu**[5] | **Sylvio Indris**[3] | **Helmut Ehrenberg**[3] | **Xiaodong Guo**[2] | **Weibo Hua**[1,2,3]

[1]School of Chemical Engineering and Technology, Xi'an Jiaotong University, Xi'an, China

[2]School of Chemical Engineering, Sichuan University, Chengdu, China

[3]Institute for Applied Materials (IAM), Karlsruhe Institute of Technology (KIT), Eggenstein-Leopoldshafen, Germany

[4]Diffraction and Scattering Division, Japan Synchrotron Radiation Research Institute (JASRI), Kouto, Sayo-cho, Sayo-gun, Hyogo, Japan

[5]Beijing Synchrotron Radiation Facility, Institute of High Energy Physics, Chinese Academy of Sciences, Beijing, China

Correspondence

Weibo Hua, Xiaodong Guo and Helmut Ehrenberg.
Email: weibo.hua@xjtu.edu.cn, xiaodong2009@scu.edu.cn and helmut.ehrenberg@kit.edu

Funding information

Distinguished Young Foundation of Sichuan Province, Grant/Award Number: 2020JDJQ0027; National Natural Science Foundation of China, Grant/Award Numbers: 22108218, 20A20145, 21878195; German Research Foundation, Grant/Award Number: 390874152; "Young Talent Support Plan" of Xi'an Jiaotong University, Grant/Award Number: HG6J016; Qinchuangyuan Innovative Talent Project, Grant/Award Number: QCYRCXM-2022-137

Abstract

With exceptional capacity during high-voltage cycling, P3-type Na-deficient layered oxide cathodes have captured substantial attention. Nevertheless, they are plagued by severe capacity degradation over cycling. In this study, tuning and optimizing the phase composition in layered oxides through Li incorporation are proposed to enhance the high-voltage stability. The structural dependence of layered $Na_{2/3}Li_xNi_{0.25}Mn_{0.75}O_{2+\delta}$ oxides on the lithium content ($0.0 \leq x \leq 1.0$) offered during synthesis is investigated systematically on an atomic scale. Surprisingly, increasing the Li content triggers the formation of mixed P2/O3-type or P3/P2/O3-type layered phases. As the voltage window is 1.5–4.5 V, P3-type $Na_{2/3}Ni_{0.25}Mn_{0.75}O_2$ ($NL_{0.0}NMO$, $R\bar{3}m$) material exhibits a sequence of phase transformations throughout the process of (de)sodiation, that is, O3⇌P3⇌O3′⇌O3″. Such complicated phase transitions can be effectively suppressed in the $Na_{2/3}Li_{0.7}Ni_{0.25}Mn_{0.75}O_{2.4}$ ($NL_{0.7}NMO$) oxide with P2/P3/O3-type mixed phases. Consequently, cathodes made of $NL_{0.7}NMO$ exhibit a substantially enhanced cyclic performance at high voltages compared to that of the P3-type layered $NL_{0.0}NMO$ cathode. Specifically, $NL_{0.7}NMO$ demonstrates an outstanding capacity retention of 98% after 10 cycles at 1 C within 1.5–4.5 V, much higher than that of $NL_{0.0}NMO$ (83%). This work delves into the intricate realm of bolstering the high-voltage durability of layered oxide cathodes, paving the way for advanced sodium-ion battery technologies.

KEYWORDS

high-voltage cycling, Li incorporation, phase transition, sodium ion batteries, triphasic composites

1 | INTRODUCTION

Given their cost-effectiveness and abundant resources, sodium-ion batteries (SIBs) are emerging as an exceptionally promising substitute for conventional lithium-ion batteries.[1–3] Cathode materials, as one of the pivotal constituents of SIB systems, wield a dominant influence over cost efficiency and energy density. Among diverse cathode materials like transition-metal (TM) oxides (Na_xTMO_2) ($x < 1$),[4] polyanion compounds,[5] Prussian blue analogs,[6] and organic compounds,[7] layered oxides have captured significant attention, owing to their distinctive two-dimensional structure that facilitates the facile (de)insertion of Na^+. Notably, among these layered oxides, the Mn-based P-type variants have emerged as particularly advantageous for practical, large-scale applications.[8] Based on the TM-O stacking sequence and electrochemical environments of Na^+, layered Na_xTMO_2 can be classified into three distinct phases: P2, P3, and O3 phases, respectively.[9] Despite O-type Na_xTMO_2 demonstrating a high capacity owing to its elevated sodium component, it often exhibits unsatisfactory rate property and cycling stability. This can be associated with the hindered kinetics of sodium ion transfer resulting from unfavorable diffusion pathways for Na^+ ions. In sharp contrast, P-type Na_xTMO_2 materials exhibit remarkable rate capability and exceptional long-term cycling performance, primarily attributed to open prismatic diffusion pathways. Among P-type Na_xTMO_2 materials, P3-type oxides are stable under a low temperature (<800°C), indicating lower energy consumption for synthesis, while P2-type counterparts usually generate at 900°C.[10] In general, compared with P2-type compounds, P3-type oxides deliver a higher capacity.[11] Nevertheless, at an elevated voltage of 4.4 V, P3-type cathode materials undergo irreversible phase transition, that is, O3⇌P3,[12] consequently resulting in a swift deterioration of capacity.

To address this challenge, recent research has focused on the binary or ternary mixed-phase layered oxides, which can amalgamate the advantages of single-phase materials while mitigating their inherent limitations. Typically, introducing TM cations is an effective method to synthesize composite-layered structures.[13] For instance, Cheng et al.[14] introduced Ti^{4+} into the TM layer, obtaining the biphasic compound, $Na_{0.76}Ni_{0.33}Mn_{0.5}Fe_{0.1}Ti_{0.07}O_2$, including O3 (41.09 wt%) and P2 (58.91 wt%) phases, demonstrating exceptional cycling performance with a remarkable capacity retention of 75.4% after 500 cycles. Similarly, with the introduction of Zn^{2+} and Cu^{2+} into the TM layer, P2/P3 biphasic $Na_{0.78}Cu_{0.27}Zn_{0.06}Mn_{0.67}O_2$ was developed, which exhibits superior cycling stability.[15] Recently, a triphasic composite, $Na_{0.5}Co_{0.15}Mn_{0.65}Mg_{0.1}O_2$,[16] consisting of P2/P3/spinel phases, was developed by substituting Mg^{2+}, delivering excellent electrochemical characteristics. However, the impact of element dopant on the formation mechanism of multiphase composites is still unclear. Similarly, the role of mixed-phase compounds in structural stability is not well understood.

In this study, Li-substituted layered composites, $Na_{2/3}Li_xNi_{0.25}Mn_{0.75}O_{2+\delta}$ ($0.0 \le x \le 1.0$), with binary (P2/P3) or ternary (P2/P3/O3) phases were synthesized. A small amount of Li ions ($x < 0.2$) in the compounds produces a P3-type layered structure. With increasing Li concentration, two- or three-phase composite structures emerge, namely mixed P2/O3-type or P3/P2/O3-type layered structures, which are novel and unprecedented. P3-type $Na_{2/3}Ni_{0.25}Mn_{0.75}O_2$ undergoes multiple phase transformations, that is, O3⇌P3⇌O3′⇌O3″, during the (de)sodiation process within 1.5–4.5 V. Remarkably, these complex phase transformations are effectively suppressed in the mixed P3/P2/O3-type oxide cathodes upon (de)sodiation within 1.5–4.5 V. Consequently, $NL_{0.7}NMO$ undergoes a remarkable improvement in the electrochemical performance, with 98% retention rate after 10 cycles at a current density of 1 C within 1.5–4.5 V, higher than that of $NL_{0.0}NMO$ (83%). This study presents novel insights and innovative strategies aimed at enhancing the electrochemical property of layered oxide cathode materials.

2 | RESULT AND DISCUSSION

Using a solid-state calcination method,[17–22] Li-incorporated oxides, $Na_{2/3}Li_xNi_{0.25}Mn_{0.75}O_{2+\delta}$ ($0.0 \le x \le 1.0$), were prepared by sintering the mixture of Na_2CO_3, a hydroxide precursor and varying amounts of $LiOH \cdot H_2O$. The synthesized materials were labeled as $NL_{0.0}NMO$, $NL_{0.1}NMO$, $NL_{0.2}NMO$, $NL_{0.3}NMO$, $NL_{0.4}NMO$, $NL_{0.5}NMO$, $NL_{0.7}NMO$, and $NL_{1.0}NMO$, respectively. The oxygen content (δ value) was correspondingly augmented to keep the electroneutrality of these prepared materials. The powder X-ray diffraction (XRD) patterns, as well as the Rietveld refinements, of $Na_{2/3}Li_xNi_{0.25}Mn_{0.75}O_{2+\delta}$ oxides are illustrated in Figure 1A, Figure S1 and Table S1. The XRD patterns of $NL_{0.0}NMO$ and $NL_{0.1}NMO$ unequivocally demonstrate that they are both single P3-type layered phases ($R\bar{3}m$). From $NL_{0.2}NMO$ to $NL_{0.7}NMO$, all the compounds are found to be a mixture of the P3-type ($R\bar{3}m$), P2-type ($P6_3/mmc$), and O3-type layered phases ($C2/m$). Rietveld refinement results show that, as the Li content augments, the weight proportion of the P3 phase starts at 100% for $NL_{0.0}NMO$, progressively diminishing to approximately 10% for $NL_{0.4}NMO$, while the fraction of P2-type and O3-type layered phases gradually increases to ~67% and ~23%,

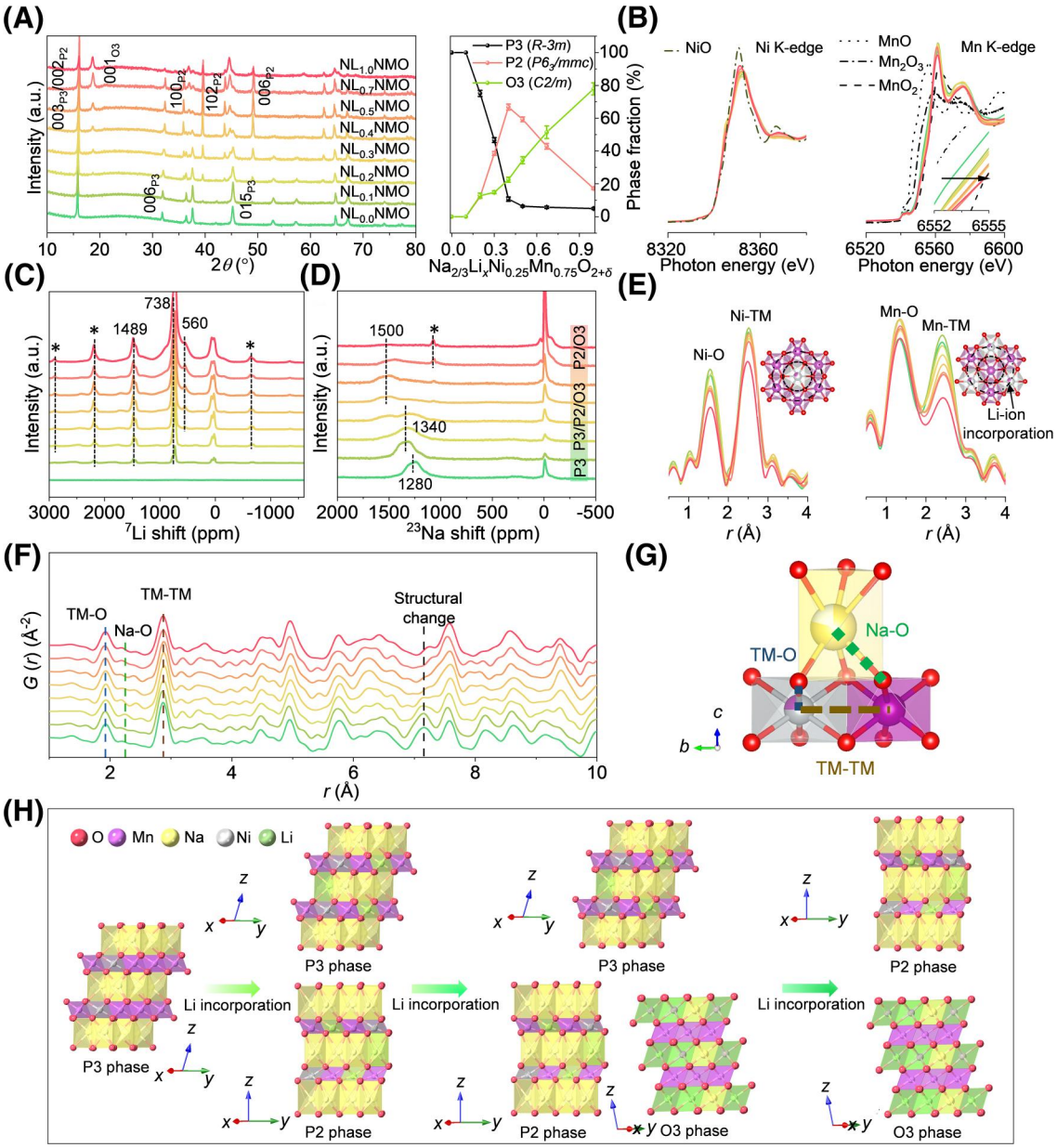

FIGURE 1 Li-incorporation-induced structural alterations in $Na_{2/3}Li_xNi_{0.25}Mn_{0.75}O_{2+\delta}$ ($0.0 \le x \le 1.0$). (A) XRD patterns of $Na_{2/3}Li_xNi_{0.25}Mn_{0.75}O_{2+\delta}$ oxides and the corresponding weight fraction of various layered phases with increasing Li content; (B) Ni, Mn K-edge XANES spectra of samples; (C) ^{7}Li and (D) ^{23}Na ss-NMR spectra (asterisks represent spinning sidebands); (E) Fourier transformation of the EXAFS spectra at Ni and Mn K-edges; the insets showcase the TM layer encircling the absorbing Ni or Mn atoms in the layered structure, respectively. (F) PDF analysis and (G) the corresponding local structure model; (H) the schematic representation of structural changes of $Na_{2/3}Li_xNi_{0.25}Mn_{0.75}O_{2+\delta}$ with increasing Li contents ($0.0 \le x \le 1.0$). EXAFS, extended X-ray absorption fine structure; PDF, pair distribution function; ss-NMR, solid-state nuclear magnetic resonance; TM, transition-metal; XANES, X-ray absorption near edge structure; XRD, X-ray diffraction.

respectively, see Figure 1A and Figure S2. As the supplied Li content surpasses 0.4, the percentage of the P2-type layered phase gradually declines, while the portion of the O3-type layered phase increases, which suggest a transformation from the P2-type to O3-type layered phase. Correspondingly, the structural changes of $Na_{2/3}Li_xNi_{0.25}Mn_{0.75}O_{2+\delta}$ induced by Li incorporation are illustrated in Figure 1H. It is worthy to note that the phase transformation from P3- to P2-type phase generally occurs at an elevated temperature (>900°C). The obtained results suggest that the incorporation of Li, in addition to Na, could facilitate the generation of the P2-type phase at a comparatively lower temperature (i.e., 700°C).

As depicted in Figure S3, scanning electron microscopy (SEM) clarifies that as-synthesized samples are flake-shaped particles in a size of approximately 500–600 nm. The surface of these flake-shaped crystals exhibits several fine crystallites, the number of which increases with higher Li concentration,

possibly due to the generation of the O3 phase. Energy-dispersive spectroscopy mappings (Figures S4–S11) demonstrate that Na, Ni, Mn, and O elements distribute homogenously in the particle interior. X-ray absorption spectroscopy (XAS) was applied to investigate the changes of valence and local structure of $Na_{2/3}Li_xNi_{0.25}Mn_{0.75}O_{2+\delta}$ ($0.0 \le x \le 1.0$). Figure 1B exhibits the Ni, Mn K-edge X-ray absorption near edge structure (XANES) spectra of all samples. No substantial alterations were discernible in the Ni K-edge XANES spectra of these samples, all were assigned to Ni^{2+}. In contrast to Ni, the oxidation state of manganese exhibits a marginal increment, that is, ranging from around +3.8 in $NL_{0.0}NMO$ to +4.0 in $Na_{2/3}Li_xNi_{0.25}Mn_{0.75}O_{2+\delta}$ oxides with higher Li contents ($x \ge 0.3$). Figure 1E showcases the Fourier-transformed Ni and Mn K-edge extended X-ray absorption fine structure (EXAFS) spectra of as-prepared compounds. In all samples, Ni and Mn K-edge EXAFS spectra manifest two prominent peaks, located approximately at 1.65 and 2.60 Å, corresponding to the first TM–O coordination shell and the second coordination shell of TM–TM, respectively.[23] Compared with the coordination shell of Ni–TM, the intensity of Mn–TM peak significantly drops with Li incorporation, which implies that Li-ions are more likely encompassed by Mn ions ($r_{Mn^{4+}} = 0.53$ Å), that is, positioned on the Ni sites because of their similar ionic radius ($r_{Li^+} = 0.76$ Å, $r_{Ni^{2+}} = 0.69$ Å).[24,25]

The local structures of all compounds were further examined by solid-state nuclear magnetic resonance (ss-NMR) spectroscopies of ^{7}Li and ^{23}Na. As depicted in Figure 1C, in the ^{7}Li ss-NMR spectra of these oxides, the narrow resonance at ~0 ppm can be indexed to surface-deposited diamagnetic Li species such as Li_2CO_3 and LiOH. Since both $NL_{0.0}NMO$ and $NL_{0.1}NMO$ oxides possess a single P3-type layered phase, the major resonance observed at ~738 ppm in $NL_{0.1}NMO$ is most likely associated with Li ions at the Na sites. The NMR peaks centered at ~1489 ppm can be assigned to Li-ions at the TM sites.[26,27] From $NL_{0.2}NMO$ to $NL_{1.0}NMO$, the main NMR peaks exhibit negligible changes in position, which implies a consistent local environment of Li ions within the P3-, P2-, and O3-type layered phases. Interestingly, a new resonance appeared at ~560 ppm in the NMR spectra of $Na_{2/3}Li_xNi_{0.25}Mn_{0.75}O_{2+\delta}$ oxides with higher Li contents ($x \ge 0.3$), which is probably attributed to the generation of P2/O3-type phases.[28] Figure 1D illustrates the ^{23}Na ss-NMR spectra of these samples. The sharp peak near 0 ppm is again arising from diamagnetic impurities like Na_2CO_3 and NaOH.[27,29] The broad NMR peak at around 1280 ppm of $NL_{0.0}NMO$ can stem from the Na-ions in the Na layer of P3-type structure.[30,31] This signal shifts to 1340 ppm as the Li content increases to 0.2, possibly due to a potential rise in the Mn valence state from $Mn^{\sim 3.8+}$ to Mn^{4+} (see XANES results in Figure 1B). The occurrence of an NMR signal at ca. 1500 ppm and the disappearance of the peak at 1340 ppm from $NL_{0.2}NMO$ to $NL_{1.0}NMO$ reveal the structure evolution from P3- to P3/P2/O3- and finally P2/O3-type phases.[32] The weak ^{23}Na NMR signal observed for $NL_{1.0}NMO$ is caused by extreme line broadening (see Figure S12).

To investigate the real-space interatomic distances of the synthesized oxides, the total scattering pair distribution function (PDF) technique was employed, as illustrated in Figure 1F, Figures S13 and S14. The peaks of $G(r)$ at about 7.20 Å exhibit a weakening trend with increasing Li content, which is possibly ascribed to the decrease in the percentage of the P3-type layered phase, corresponding to the aforementioned XRD findings. The variation in the small r range (<4.00 Å) is barely observable due to the similar local structures of P3, P2-, and O3-type layered phases, see Figure S14. The first PDF signal at approximately 1.90 Å illustrates the Li/Ni/Mn-O pair correlation lengths within the TMO_6 octahedra and the subsequent peak located at ~2.90 Å signifies the Li/TM-Li/TM distances (see Figure 1F,G).[33] A minor peak at 2.27 Å denotes the interaction between O and Na in the NaO_6 prismatic cage.[34]

To unravel the intricate correlation between electrochemical property and crystallographic structure, the electrochemical tests of these cathode materials were firstly conducted on the coin cells within 2.0–4.0 V. Several voltage plateaus and redox peaks can be discerned in the galvanostatic charge/discharge (GCD) voltage curves and related dQ/dV profiles of $NL_{0.0}NMO$ electrode (Figures S15 and S16), which is closely tied to the local structural transitions of Na/vacancy orderings.[35] Generally, the electrochemical profiles of cathode materials with mixed phases would exhibit their individual characteristics (potential plateaus) such as layered/spinel heterostructured Li-rich oxide materials[36] and layered tunnel hybrid cathodes.[37,38] Very interestingly, the GCD profiles of electrodes with high Li content such as $NL_{0.3}NMO$, $NL_{0.5}NMO$, and $NL_{0.7}NMO$ lack clear plateaus due to the suppressed phase transition in the layered P3/P2/O3-type composites (see in situ synchrotron-based X-ray diffraction (sXRD) results given below). Very importantly, the average working voltage of $NL_{0.2}NMO$, $NL_{0.3}NMO$, and $NL_{0.4}NMO$ electrodes is higher than that of the $NL_{0.0}NMO$ electrode, indicating a significant voltage increase following Li incorporation. For instance, the $NL_{0.3}NMO$ cathode delivers the highest initial discharge capacity of 94 mAh g^{-1} and the highest voltage plateau at ca. 3.1 V at a rate of 0.1 C. The rate capabilities of all electrodes were measured ranging from 0.1 to 10 C. $NL_{0.4}NMO$ cathode demonstrates the optimum rate capability, with a discharge capacity of around 84 mAh g^{-1} even at 10 C

(Figure S17). Figure S18 provides the cyclic property of selected cathodes at a current density of 0.1 C. During the initial 40 cycles, a gradual increase in the discharge capacities of the $NL_{0.7}NMO$ and $NL_{1.0}NMO$ cathodes is observed, which is attributed to a gradual activation process. After 100 cycles, other six cathodes exhibit an outstanding capacity retention of nearly 100% at 0.1 C, indicating an exceptional cyclic stability within 2.0–4.0 V. However, $NL_{0.0}NMO$ electrode displays an inferior cycling property at 1 C over 250 cycles compared to other electrodes (Figure S19). The capacity retention of the $NL_{0.2}NMO$, $NL_{0.5}NMO$, and $NL_{0.7}NMO$ cathodes is 93%, 96%, and 97%, respectively, surpassing that of the $NL_{0.0}NMO$ cathode (82%). Therefore, Li incorporation significantly improves the long-term cyclic stability in Mn-based-layered Na cathode materials.

To explore the influence of lithium incorporation on the structural stability and electrochemical behavior of the prepared cathode materials upon high-voltage cycling, electrochemical measurements were carried out on the fabricated coin cells within 1.5–4.5 V. The initial charge/discharge voltage plots of all cathodes at 0.1 C demonstrate distinct characteristics as displayed in Figure 2A. Obviously, the discharge curve of the $NL_{0.0}NMO$ electrode exhibits a long plateau at approximately 1.9 V owing to the reduction of Mn^{4+}. By contrast, the voltage platforms observed at 4.2 and 1.9 V exhibit a gradual reduction in length as the Li amount in the layered oxides increases, indicating relatively minor structural changes in the Li-incorporated oxides during high-voltage operation. Figure 2B presents the dQ/dV curves of $NL_{0.0}NMO$ and $NL_{0.7}NMO$. Four pairs of redox peaks between 3.0 and 4.2 V can be observed in the dQ/dV plot of the $NL_{0.0}NMO$ cathode, which represent the reduction/oxidation of Ni^{2+}/Ni^{4+} coupled with the Na^+/vacancy ordering/rearrangement. The presence of a flat voltage plateau and a noticeable peak in dQ/dV profile at approximately 4.2 V can be assigned to the O^{2-}/O^{n-}

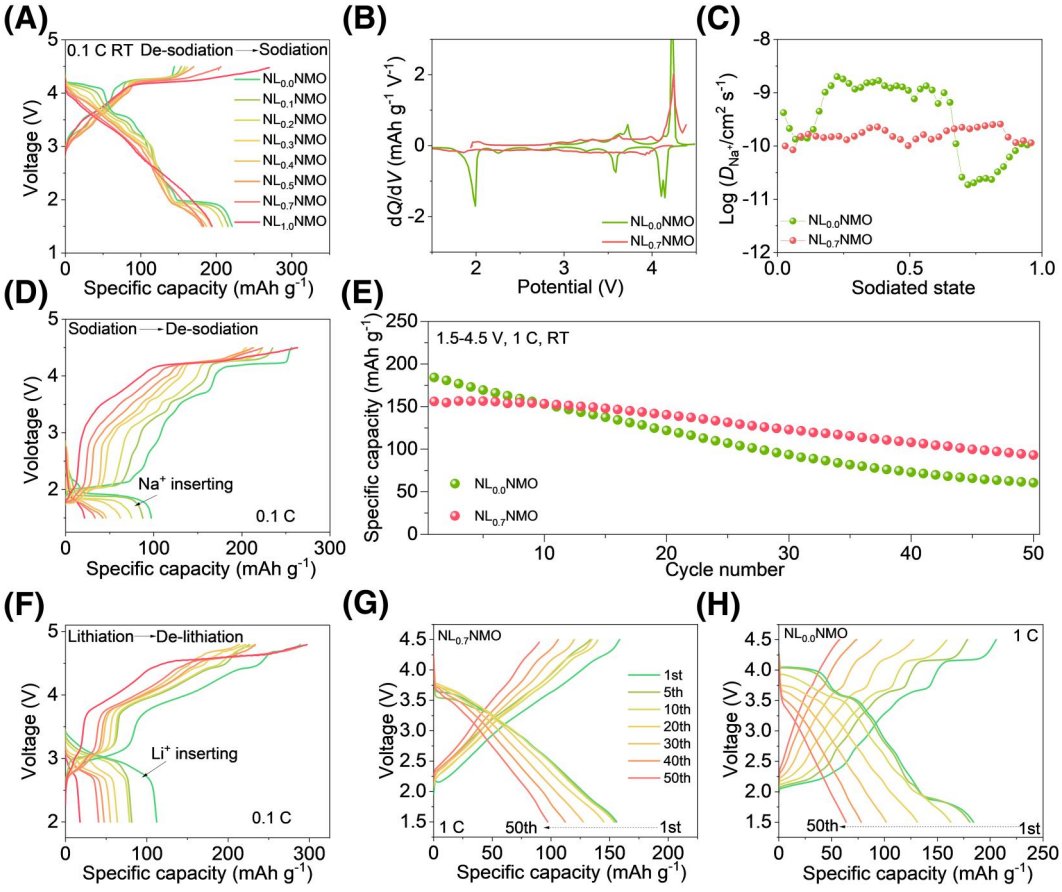

FIGURE 2 Electrochemical performance of coin cells for $Na_{2/3}Li_xNi_{0.25}Mn_{0.75}O_{2+\delta}$ cathodes during the (de)intercalation of Na/Li-ions. (A) The first charge/discharge profiles for $Na/Na_{2/3}Li_xNi_{0.25}Mn_{0.75}O_{2+\delta}$ cells within 1.5–4.5 V without predischarge at 0.1 C; (B) the corresponding dQ/dV profiles; (C) the D_{Na^+} values calculated from GITT during the second cycle within 1.5–4.5 V; (D) the first discharge/charge curves of $Na/Na_{2/3}Li_xNi_{0.25}Mn_{0.75}O_{2+\delta}$ cells with predischarge at 0.1 C; (E) cycling property for $NL_{0.0}NMO$ and $NL_{0.7}NMO$ cells at 1 C within 1.5–4.5 V; (F) the initial GCD profiles with predischarge of $Li/Na_{2/3}Li_xNi_{0.25}Mn_{0.75}O_{2+\delta}$ cells at 0.1 C within 2.0–4.8 V; GCD curves of (G) $NL_{0.7}NMO$ and (H) $NL_{0.0}NMO$ cathodes selected at various cycles at 1 C. GCD, galvanostatic charge/discharge; GITT, galvanostatic intermittent titration technique; RT, room temperature.

redox switching in the $NL_{0.0}NMO$ electrode.[39] Na^+ diffusion kinetics in the cathodes was evaluated using the galvanostatic intermittent titration technique (GITT). Figures S20–S27 display the second charge/discharge curves of $Na_{2/3}Li_xNi_{0.25}Mn_{0.75}O_{2+\delta}$ electrodes measured by GITT at 26 mA g^{-1}. The Na-ion diffusion coefficient (D_{Na^+}) was calculated according to equation (1)[40–42] (Supporting Information S1). Intriguingly, the D_{Na^+} value of $NL_{0.7}NMO$ remains relatively stable during the insertion of Na ions (see Figure 2C), while the Na^+ diffusion coefficient of $NL_{0.0}NMO$ changes between 10^{-11} and 10^{-9} cm^2 s^{-1}, especially in the phase transition regions.

In order to determine the quantity of Na vacancies (□) present in the layered oxides, all cathodes were discharged to 1.5 V initially, followed by charging to 4.5 V. As illustrated in Figure 2D, $NL_{0.0}NMO$ electrode exhibits the maximum initial discharge capacity, reaching 97 mAh g^{-1}, associated with about one-third Na ion intercalation into the $Na_{2/3}Ni_{0.25}Mn_{0.75}O_2$. The initial discharge capacity gradually decreases as Li content increases in $Na_{2/3}Li_xNi_{0.25}Mn_{0.75}O_{2+\delta}$ oxides, indicating that Li ions progressively occupy the Na vacancies in the synthesized materials. To extend the application of these materials, the prepared oxides were utilized as cathode materials in Li-ion batteries (LIBs) (Figure 2F). The fabricated coin cells were also firstly discharged to 2.0 V to further confirm the amount of Na vacancies in the layered structures, as depicted in Figure 2F. A reduced first discharge capacity is found as the Li concentration rises, aligning precisely with the electrochemical results in Figure 2D. The shape of charge-voltage profiles for these cathodes are similar to those of Li- and Mn-rich oxide cathodes (LMROs).[28] Figure S28 exhibits the cycling performance (2.0–4.8 V) of these materials with predischarge. Among them, the $NL_{0.7}NMO$ cathode stands out with a remarkable capacity retention rate of 77% after 50 cycles, which is higher than that of $NL_{0.0}NMO$ cathode (63%). The charge-voltage profiles without predischarge are shown in Figure S29, and they resemble those of LMROs.[43] Figure S30 manifests the cycling performance of all cathodes within 2.0–4.8 V. Surprisingly, $NL_{0.0}NMO$ cathode without the predischarge process exhibits a worse cycling property compared to the discharge–charge tests in Figure S28. The capacity retention of $NL_{0.0}NMO$ cathode is 55% after 50 cycles, which is lower than that of $NL_{0.7}NMO$ cathode (76%). These results confirm that the as-synthesized oxides with P3/P2/O3-type multiphase (e.g., $NL_{0.7}NMO$) demonstrate an enhanced high-voltage cycling stability when used as cathode materials in both LIBs and SIBs.

The cyclic performances for $NL_{0.0}NMO$ and $NL_{0.7}NMO$ cathodes were evaluated over a wide voltage scope of 1.5–4.5 V at 0.1 and 1 C, see Figure 2E and Figure S31. As depicted in Figure 2E, although the $NL_{0.0}NMO$ cathode demonstrates an impressive initial discharge capacity (184 mAh g^{-1}), it undergoes severe capacity fading upon cycling, resulting in only 83% capacity retention after 10 cycles. Very importantly, approximately 98% of the initial discharge capacity of $NL_{0.3}NMO$, $NL_{0.4}NMO$, $NL_{0.5}NMO$, and $NL_{0.7}NMO$ cathodes can be maintained after 10 cycles at both 0.1 and 1 C (see Figure S31). Such high capacity retention is superior to those reported values for P3-type layered oxides,[10,11,44–47] P2-type layered oxides,[48–51] O3-type layered oxides,[3,49,52,53] and layered oxides with mixed P2/P3/O3 structures,[13,39,49,54] see Tables S2 and S3. The practical energy density of the $NL_{0.7}NMO$ cathode is approximately 423 Wh kg^{-1} after 10 cycles, which is comparable to that of $LiFePO_4$[55,56] and $LiMn_2O_4$[57] cathode materials for LIBs (~410 Wh kg^{-1}), indicating promising applications for high-energy SIBs. Unfortunately, a gradual attenuation of the discharge capacities is observed in $NL_{0.3}NMO$, $NL_{0.4}NMO$, $NL_{0.5}NMO$, and $NL_{0.7}NMO$ cathodes over the subsequent 40 cycles, which is attributed to the serious irreversible structural damage and release of lattice oxygen from the oxides in this wide voltage region (as discussed subsequently with regard to the ex situ XRD and XAS findings of fatigued electrodes after various cycles).

The evolution of structure in P3-type $NL_{0.0}NMO$ upon the first cycle within 1.5–4.5 V was investigated by in situ XRD (Ag Kα radiation). When Na ions extract from the P3-type $NL_{0.0}NMO$, the reflection assigned to 001_{P3} moves to lower two-theta angles, which indicates an expansion of the interlayer spacing stemming from enhanced electrostatic repulsion between contiguous oxygen ions, see Figure 3A. Simultaneously, 130_{P3} reflection shifts toward higher scattering angles, demonstrating that the *ab* plane contracts as a result of the oxidation of Ni^{2+}. With an increase in voltage from 3.0 to 4.0 V, P3 phase partially transforms to the O3′ phase (space group *C*2/*c*), evidenced by the emergence of $311_{O3'}$ reflection. When the cell is charged to 4.3 V, a new reflection assigned to $003_{O3''}$ generates at the expanse of $311_{O3'}$ and 001_{P3} peaks, indicating that P3 and O3′ phases completely transform to O3″ phase (space group $R\bar{3}m$). Further, Na-ion intercalation results in the transformation from the O3″ structure back into the O3′ and P3 phases. As the voltage diminished to 1.9 V, a new O3 phase (space group $R\bar{3}m$) appears accompanied by the vanishing of P3 phase, which is supported by the appearance of 001_{O3} reflection along with the absence of reflections belonging to the P3 phase. Therefore, P3-type $NL_{0.0}NMO$ experiences a sequence of phase transitions upon (de)sodiation within 1.5–4.5 V, that is, O3⇌P3⇌O3′⇌O3″. The corresponding changes of phase fractions upon the first (de)sodiation are illustrated in Figure 3C. Furthermore, to elucidate the

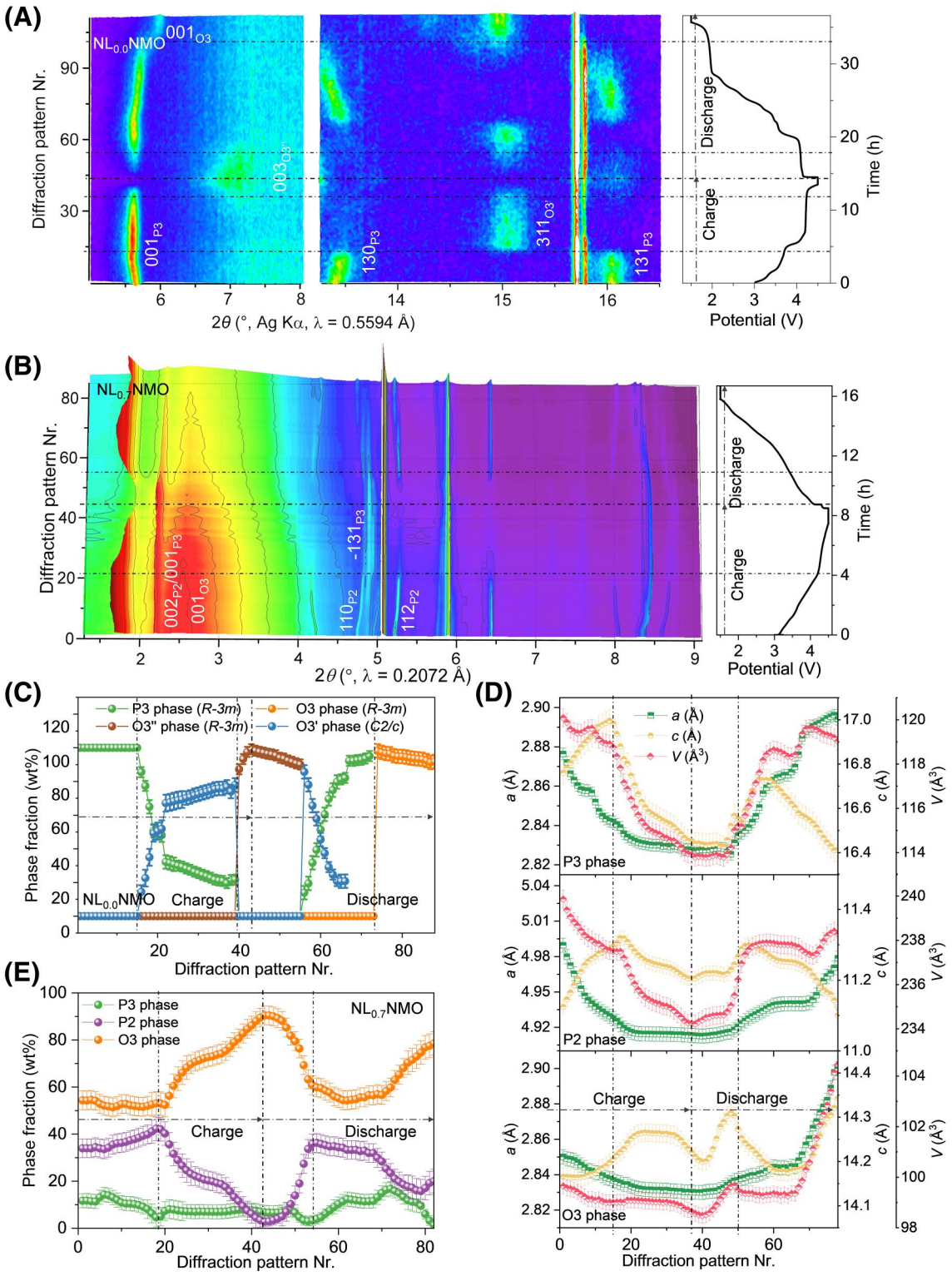

FIGURE 3 Na-driven structural changes of P3-type layered $NL_{0.0}NMO$ and mixed P3/P2/O3-type layered $NL_{0.7}NMO$ electrodes during Na^+ extraction/insertion. (A) In situ XRD patterns of $Na/NL_{0.0}NMO$ cells upon the first (de)sodiation within 1.5–4.5 V, right side of the figure contains the corresponding GCD curves; (B) 3D maps of in situ sXRD patterns of $NL_{0.7}NMO$ versus Na cells upon the first (de)intercalation of Na^+ at a rate of 0.1 C, with the relevant GCD curve on the right; (C) phase fraction variations of $NL_{0.0}NMO$ electrode during cycling; the variations in (D) lattice parameters (*a*, *c*, and *V*) and (E) phase fractions for the $NL_{0.7}NMO$ electrode during cycling. GCD, galvanostatic charge/discharge; XRD, X-ray diffraction.

enhanced cyclic performance of $Na/NL_{0.7}NMO$, in situ sXRD patterns were captured at C/10 within 1.5–4.5 V. As depicted in Figure 3B, only alterations in both position and intensity of all reflections can be detected upon Na^+ extraction/intercalation, suggesting the mitigation of multistep phase transformation upon high-voltage cycling. The dynamic evolution of phase fractions throughout the initial charge/discharge cycle

is illustrated in Figure 3E. The weight fraction of the P2-type phase slightly increases until the charge voltage reaches 4.2 V accompanied by the disappearence of the P3-type layered phase. During the charging process of up to 4.5 V, the percentage for the O3-type layered phase increases from 54.3% to 78.5% while the content of the P2-type phase decreases from 34.0% to 20.0%, suggesting a gradual P2-O3 phase transition in the oxygen-involved voltage plateau (see X-ray photoelectron spectroscopy (XPS) spectra of charged $NL_{0.7}NMO$ electrode in Figure 4). When the voltage decreased to 3.5 V, the proportions of P2- and O3-type layered phases attempt to return to their initial values. With the gradual insertion of more Na-ions into the layered structures (below 2.0 V), the weight fraction of the O3-type phase gradually increases with a decrease in the relative percentage of both P2- and P3-type phases. The alterations in lattice parameters *a*, *c*, and unit-cell volume (*V*) for P2-type, P3-type, and O3-type phases upon charge/discharge are illustrated in Figure 3D. Upon charging to 4.2 V, a noticeable increase is observed in the parameter *c* of three-layered phase rises, while the parameter *a* gradually reduces, indicating that all the three phases participate in the oxidation reaction. At a higher voltage of 4.5 V, the parameter *a* of all three phases does not undergo significant changes. With more Na ions extracting from $NL_{0.7}NMO$, the parameter *c* of P2- and P3-type layered phases experiences a gradual decline. The lattice parameter *c* of the O3-type phase remains nearly constant and then slightly drops during the lattice oxygen oxidation process, which aligns with the changes in the LMROs during cycling.[18] The P2-type and P3-type phases demonstrate minor variations in unit-cell volume (*V*) before and after one complete cycle, with percentages of 0.9% and 0.7%, respectively, which both surpass that of the O3-type phase (4.8%). The comparatively small volume change also illustrates the superior structural stability stemming from the Li incorporation. Significantly, unlike $NL_{0.0}NMO$, no new phase is formed in $NL_{0.7}NMO$ during wide voltage operation, which is probably because the as-synthesized P3/P2/O3-type phases in $NL_{0.7}NMO$ could transform between these phases at different voltages. The suppression of the complicated phase transformations, thereby, promotes the cyclic capability and rate performance of $NL_{0.7}NMO$ (see Figure 2, Figure S32). Additionally, in situ sXRD findings of a Li/$NL_{0.7}NMO$ cell demonstrate the remarkable capability of $NL_{0.7}NMO$ cathode in

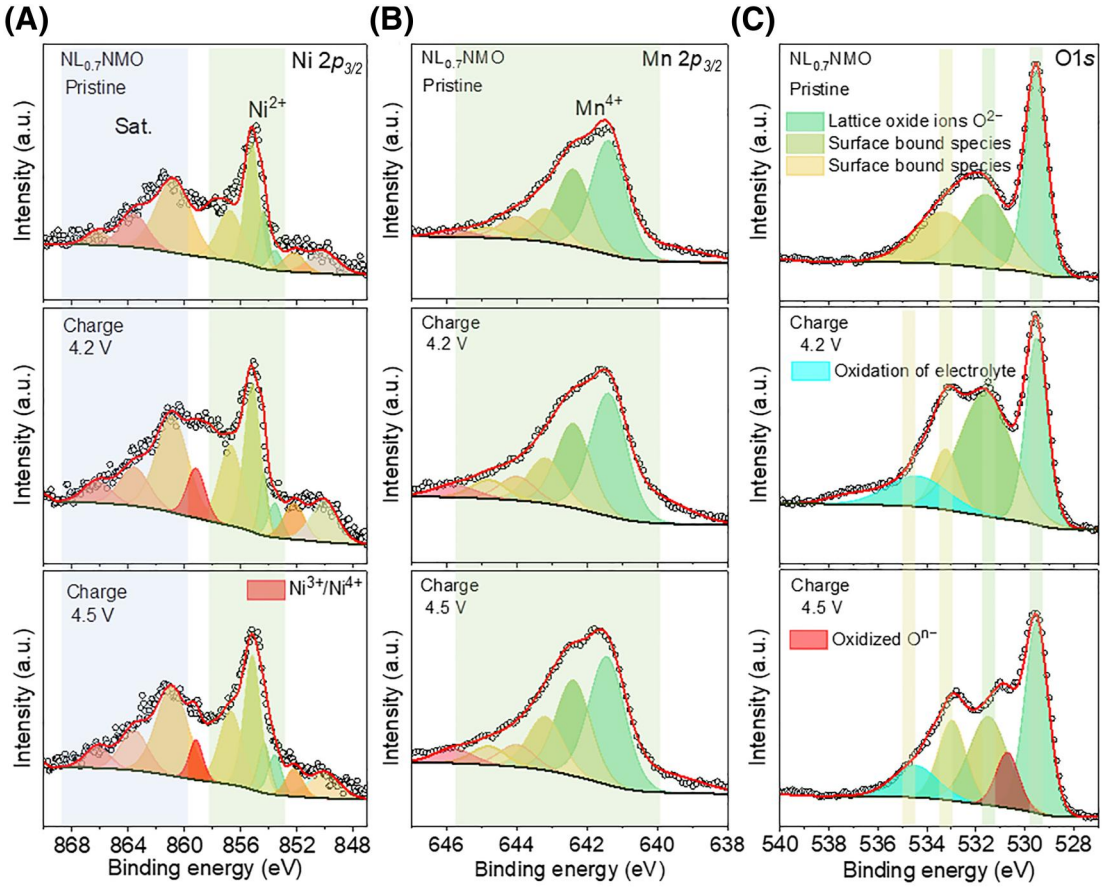

FIGURE 4 XPS spectra for $NL_{0.7}NMO$ in different charge states: pristine, 4.2 and 4.5 V of (A) Ni $2p_{3/2}$, (B) Mn $2p_{3/2}$, and (C) O1*s*. XPS, X-ray photoelectron spectroscopy.

accommodating lithium ions reversibly within 2.0–4.8 V, see Figure S33.

To unravel the intricate charge compensation mechanism for $NL_{0.7}NMO$ upon charge, XPS analyses were carried out. Figure 4A exhibits the Ni $2p_{3/2}$ XPS spectra of $NL_{0.7}NMO$ electrode at different states of charge. For the pristine electrode, the adjacent multiple peaks corresponding to Ni^{2+} and satellite signals can be observed. Notably, a new peak (highlighted in red) emerges at 859.2 eV in the Ni $2p_{3/2}$ profiles at both 4.2 and 4.5 V, which is assigned to Ni^{3+}/Ni^{4+}.[58] The multiple peaks in Mn $2p_{3/2}$ spectra (Figure 4B) are indexed to Mn^{4+} during the whole charge process,[59,60] confirming that Mn^{4+} has no activity within 2.0–4.5 V. As shown in Figure 4C, the peaks at 531.9 and 533.1 eV in O1*s* spectra are connected with surface oxide species, like oxygen in hydroxides and carbonates, respectively. Furthermore, the discernible signal centered at 529.4 eV can be ascribed to lattice oxygen (O^{2-}). However, a new peak (highlighted in red) at 530.6 eV appears subsequent to a charge of 4.5 V, demonstrating that lattice oxygen O^{2-} was oxidized to the O^{n-} during the platform region (4.2–4.5 V). Moreover, the electrolyte oxidation reaction on the cathode surface occurs at both 4.2 and 4.5 V, as substantiated by the discernible emergence

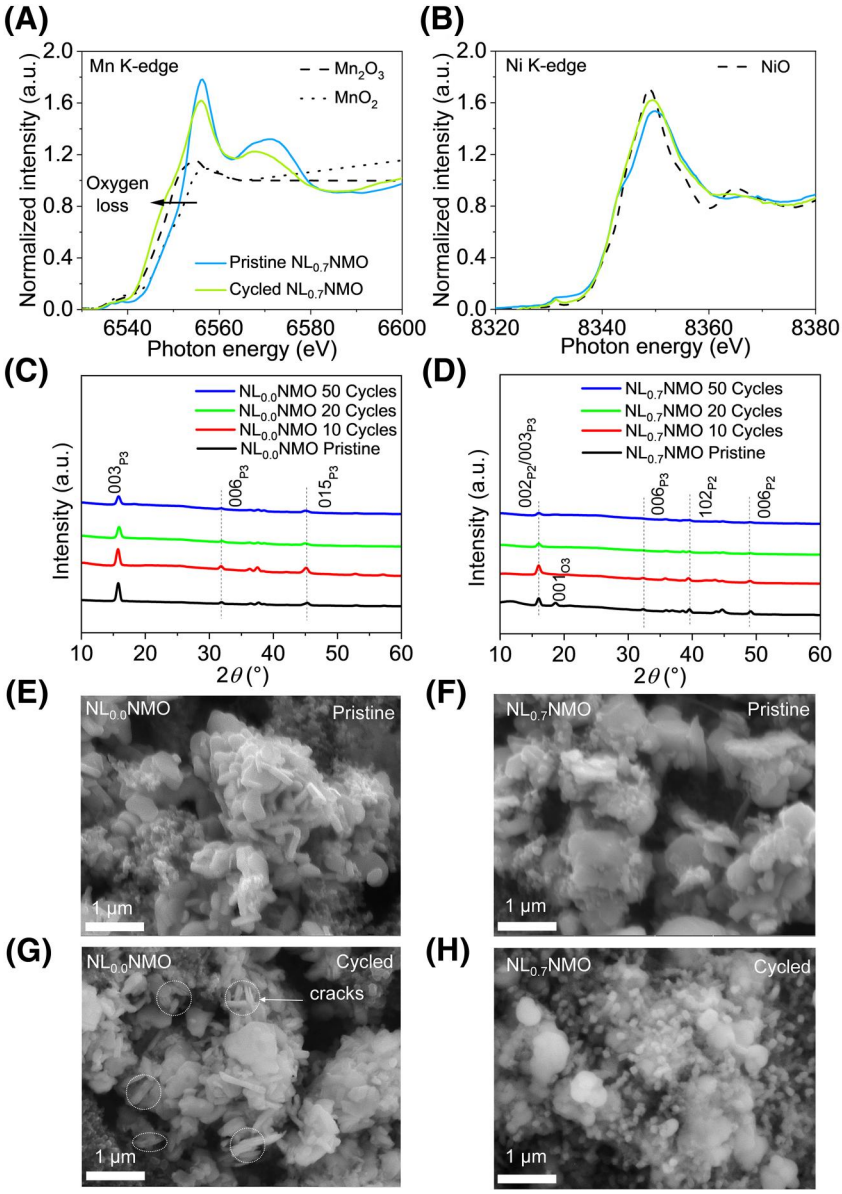

FIGURE 5 (A) Mn and (B) Ni K-edge XANES spectra of the pristine and fatigued cathodes for $NL_{0.7}NMO$; a comparison of XRD patterns for (C) $NL_{0.0}NMO$ and (D) $NL_{0.7}NMO$ electrodes before and after cycling; SEM images for $NL_{0.0}NMO$ (E) before and (G) after cycling; and SEM images of $NL_{0.7}NMO$ (F) before and (H) after cycling. SEM, scanning electron microscopy; XANES, X-ray absorption near edge structure; XRD, X-ray diffraction.

of a prominent peak at 534.8 eV in the O1*s* profiles. The XPS findings signify that the Ni^{2+}/Ni^{4+} redox couple provides a capacity within 2.0–4.2 V, while the charge compensation mechanism is facilitated by oxygen anions upon 4.2–4.5 V.

To figure out the underlying cause of capacity fading during high-voltage cycling, XRD, XAS, and SEM analyses were carried out to examine the structural and morphological alterations of fatigued electrodes following different cycles in the discharged state. The Mn and Ni K-edge XANES spectra in $NL_{0.7}$NMO after 50 cycles are depicted in Figure 5A,B. Notably, the valence state of Mn ions experienced a noteworthy reduction from +4 to +3 in the fatigued $NL_{0.7}$NMO cathode, suggesting the significant release of oxygen during high-voltage cycling. However, the Ni K-edge XANES spectra of $NL_{0.7}$NMO cathode following 50 cycles exhibit a striking resemblance to their initial electrode, indicating the persistent valence state of Ni as +2 (Figure 5B). As displayed in Figure 5C,D and Figures S34–S39, all reflections in the XRD patterns of cycled cathodes are progressively broadened and weakened with increasing cycles compared to those of pristine electrodes, indicating severe structural degradation during cycling. Noticeably, after 10 cycles, the reflections associated with the O3-type phase vanish in the fatigued $Na_{2/3}Li_xNi_{0.25}Mn_{0.75}O_{2+\delta}$ cathodes with higher Li contents ($x \geq 0.3$), which can be attributed to the gradual depletion of Li upon cycling.[26] These findings underscore the beneficial role of the O3-type layered phase in augmenting the property of layered oxide cathodes during high-voltage cycling, as evidenced by the rapid capacity fading of mixed P3/P2/O3-type layered cathodes after the disappearance of the O3-type phase, as illustrated in Figure 2E. Furthermore, in $NL_{0.7}$NMO and $NL_{1.0}$NMO electrodes, the P3-type phase completely transforms to the P2 phase after 50 cycles, primarily due to a relatively high thermodynamic stability of the P2 phase, see Figure 5D and Figure S39. After 50 cycles, the particle cracks are clearly probed in cycled $NL_{0.0}$NMO particles, implying significant structural variations during cycling, see Figure 5E,G. However, no cracks were observed in Li-incorporated layered oxides after 50 cycles, again proving their excellent structural stability. From $NL_{0.1}$NMO to $NL_{0.5}$NMO, nanoplatelet-like grains gradually become octahedral particles (Figures S40–S44). Notably, fatigued $NL_{0.7}$NMO exhibits several fine crystals attached to the surface of large particles, which might be related to the dissolution and recrystallization of oxides upon extended cycling, see Figure 5F,H. Instead of octahedral-like crystallites, thin nanosheets form on the surface of $NL_{1.0}$NMO agglomerates after 50 cycles, see Figure S45. Overall, the large morphological changes and severe structural degradation are closely associated with the limited cycling stability of layered oxide cathodes within 1.5–4.5 V.

3 | CONCLUSION

In summary, a mixing phasic strategy induced by Li incorporation, $Na_{2/3}Li_xNi_{0.25}Mn_{0.75}O_{2+\delta}$, has been used to enhance the high-voltage cycling performance. Structural, electronic, and electrochemical characterizations of layered $Na_{2/3}Li_xNi_{0.25}Mn_{0.75}O_{2+\delta}$ oxides were systematically investigated on an atomic scale. Interestingly, a single P3-type layered phase is formed with a small amount of Li-ion incorporation ($x < 0.2$) into the compounds. Intriguingly, as the Li concentration further increases, a phase transformation occurs, giving rise to the emergence of mixed P2/O3-type or P3/P2/O3-type layered phases. These results demonstrate that the introduction of Li-ions could facilitate the generation of thermodynamically stable P2- and/or O3-type phases at a relatively low temperature (i.e., 700°C). Encouragingly, the $NL_{0.7}$NMO cathode, featuring a P3/P2/O3-type multiphase structure, exhibits an impressive capacity preservation rate of 98% following 10 cycles at 1 C within 1.5–4.5 V. This extraordinary electrochemical property of this cathode can be attributed to its remarkable ability to effectively suppress multistep phase transitions, surpassing that of the P3-type $NL_{0.0}$NMO cathode as well as surpassing most values of other layered cathode materials. The disappearance of the O3-type layered phase leads to rapid capacity fading of mixed P3/P2/O3-type cathode materials upon prolonged cycling, accompanied by a large amount of oxygen release and severe structural degradation. These findings underscore the considerable importance of the O3 phase in stabilizing the high-voltage cyclic stability of layered oxides comprised of a blend of P3/P2/O3-type phases and will inspire tremendous endeavors aimed at unlocking a potential practical application of these materials.

AUTHOR CONTRIBUTIONS

Weibo Hua conceived the idea and discussed with Xiaoxia Yang, Suning Wang, Xiaodong Guo, Helmut Ehrenberg, and Sylvio Indris; Xiaoxia Yang carried out the preparation experiments; Hang Li and Sylvio Indris performed the NMR measurements; Jochi Tseng performed the PDF measurements; Weibo Hua, Xiaoxia Yang, and Zhonghua Wu performed the synchrotron-based X-ray diffraction and absorption experiments; the data were analyzed by Xiaoxia Yang, Hang Li, Suning Wang, and Weibo Hua; Xiaoxia Yang, Weibo Hua, and Suning Wang wrote the preliminary draft with input from Xiaodong Guo, Sylvio Indris, and Helmut Ehrenberg; all authors revised the

manuscript and have given the approval to the final version of the manuscript.

ACKNOWLEDGMENTS

This research was financially supported by the National Natural Science Foundation of China (Grant No. 22108218, 20A20145, 21878195), Distinguished Young Foundation of Sichuan Province (Grant No. 2020JDJQ0027), "Young Talent Support Plan" of Xi'an Jiaotong University (HG6J016), Qinchuangyuan Innovative Talent Project (QCYRCXM-2022-137) and the German Research Foundation (DFG) (Grant No. 390874152).

CONFLICT OF INTEREST STATEMENT

The authors declare no competing financial interest.

ORCID

Xiaodong Guo https://orcid.org/0009-0007-8890-3499
Weibo Hua https://orcid.org/0000-0001-5372-4422

REFERENCES

1. Zhao C, Wang Q, Yao Z, et al. Rational design of layered oxide materials for sodium-ion batteries. *Science*. 2020;370(6517):708-711. https://doi.org/10.1126/science.aay9972
2. Yabuuchi N, Kajiyama M, Iwatate J, et al. P2-type $Na_x[Fe_{1/2}Mn_{1/2}]O_2$ made from earth-abundant elements for rechargeable Na batteries. *Nat Mater*. 2012;11(6):512-517. https://doi.org/10.1038/nmat3309
3. Xu G-L, Liu X, Zhou X, et al. Native lattice strain induced structural earthquake in sodium layered oxide cathodes. *Nat Commun*. 2022;13(1):436. https://doi.org/10.1038/s41467-022-28052-x
4. Fu F, Liu X, Fu X, et al. Entropy and crystal-facet modulation of P2-type layered cathodes for long-lasting sodium-based batteries. *Nat Commun*. 2022;13(1):2826. https://doi.org/10.1038/s41467-022-30113-0
5. Chen M, Hua W, Xiao J, et al. NASICON-type air-stable and all-climate cathode for sodium-ion batteries with low cost and high-power density. *Nat Commun*. 2019;10(1):1480. https://doi.org/10.1038/s41467-019-09170-5
6. Peng J, Zhang B, Hua W, et al. A disordered Rubik's cube-inspired framework for sodium-ion batteries with ultralong cycle lifespan. *Angew Chem Int Ed*. 2023;62(6):e202215865. https://doi.org/10.1002/anie.202215865
7. Zhang H, Gao Y, Liu XH, et al. Organic cathode materials for sodium-ion batteries: from fundamental research to potential commercial application. *Adv Funct Mater*. 2021;32(4):2107718. https://doi.org/10.1002/adfm.202107718
8. Wang K, Zhuo H, Wang J, Poon F, Sun X, Xiao B. Recent advances in Mn-rich layered materials for sodium-ion batteries. *Adv Funct Mater*. 2023;33(13):2212607. https://doi.org/10.1002/adfm.202212607
9. Li J-Y, Hu H-Y, Zhou L-F, et al. Surface lattice-matched engineering based on *in situ* spinel interfacial reconstruction for stable heterostructured sodium layered oxide cathodes. *Adv Funct Mater*. 2023;33(14):2213215. https://doi.org/10.1002/adfm.202370086
10. Jo JH, Kim HJ, Choi JU, et al. Facilitating sustainable oxygen-redox chemistry for P3-type cathode materials for sodium-ion batteries. *Energy Storage Mater*. 2022;46:329-343. https://doi.org/10.1016/j.ensm.2022.01.028
11. Zhou Y-N, Xiao Z, Han D, et al. Inhibition of the P3–O3 phase transition *via* local symmetry tuning in P3-type layered cathodes for ultra-stable sodium storage. *J Mater Chem A*. 2023;11(6):2618-2626. https://doi.org/10.1039/d2ta09277h
12. Song B, Hu E, Liu J, et al. A novel P3-type $Na_{2/3}Mg_{1/3}Mn_{2/3}O_2$ as high capacity sodium-ion cathode using reversible oxygen redox. *J Mater Chem A*. 2019;7(4):1491-1498. https://doi.org/10.1039/c8ta09422e
13. Li R, Gao J, Li J, et al. An undoped tri-phase coexistent cathode material for sodium-ion batteries. *Adv Funct Mater*. 2022;32(41):2205661. https://doi.org/10.1002/adfm.202205661
14. Cheng Z, Fan XY, Yu L, et al. A rational biphasic tailoring strategy enabling high-performance layered cathodes for sodium-ion batteries. *Angew Chem Int Ed*. 2022;61(19):e202117728. https://doi.org/10.1002/anie.202117728
15. Yan Z, Tang L, Huang Y, et al. A hydrostable cathode material based on the layered P2@P3 composite that shows redox behavior for copper in high-rate and long-cycling sodium-ion batteries. *Angew Chem Int Ed*. 2019;58(5):1412-1416. https://doi.org/10.1002/anie.201811882
16. Zhu YF, Xiao Y, Hua WB, et al. Manipulating layered P2@P3 integrated spinel structure evolution for high-performance sodium-ion batteries. *Angew Chem Int Ed*. 2020;59(24):9299-9304. https://doi.org/10.1002/anie.201915650
17. Zhang R, Yang S, Li H, Zhai T, Li H. Air sensitivity of electrode materials in Li/Na ion batteries: issues and strategies. *InfoMat*. 2022;4(6):e12305. https://doi.org/10.1002/inf2.12305
18. Yang X, Wang S, Han D, et al. Structural origin of suppressed voltage decay in single-crystalline Li-rich layered $Li[Li_{0.2}Ni_{0.2}Mn_{0.6}]O_2$ cathodes. *Small*. 2022;18(25):2201522. https://doi.org/10.1002/smll.202201522
19. Jing Z, Wang S, Fu Q, et al. Architecting "Li-rich Ni-rich" core-shell layered cathodes for high-energy Li-ion batteries. *Energy Storage Mater*. 2023;59:102775. https://doi.org/10.1016/j.ensm.2023.102775
20. Hua W, Zhang J, Wang S, et al. Frontispiece: long-range cationic disordering induces two distinct degradation pathways in Co-free Ni-rich layered cathodes. *Angew Chem Int Ed*. 2022;62(12):e202214880. https://doi.org/10.1002/anie.202381261
21. Hua W, Yang X, Casati NPM, et al. Probing thermally-induced structural evolution during the synthesis of layered Li-Na-or K-containing 3d transition-metal oxides. *eScience*. 2022;2:183-191. https://doi.org/10.1016/j.esci.2022.02.007
22. Chen J, Yang Y, Tang Y, et al. Constructing a thin disordered self-protective layer on the $LiNiO_2$ primary particles against oxygen release. *Adv Funct Mater*. 2022;33(6):2211515. https://doi.org/10.1002/adfm.202211515
23. Xiao B, Liu X, Chen X, et al. Uncommon behavior of Li doping suppresses oxygen redox in P2-type manganese-rich sodium cathodes. *Adv Mater*. 2021;33(52):e2107141. https://doi.org/10.1002/adma.202107141
24. Xu J, Lee DH, Clément RJ, et al. Identifying the critical role of Li substitution in P2–$Na_x[Li_yNi_zMn_{1-y-z}]O_2$ ($0 < x, y, z < 1$) intercalation cathode materials for high-energy Na-ion batteries. *Chem Mater*. 2014;26(2):1260-1269. https://doi.org/10.1021/cm403855t
25. Kou J, Chen L, Su Y, et al. Role of cobalt content in improving the low-temperature performance of layered lithium-rich cathode materials for lithium-ion batteries. *ACS Appl Mater Interfaces*. 2015;7(32):17910-17918. https://doi.org/10.1021/acsami.5b04514
26. Yang L, Li X, Liu J, et al. Lithium-doping stabilized high-performance P2–$Na_{0.66}Li_{0.18}Fe_{0.12}Mn_{0.7}O_2$ cathode for sodium ion batteries. *J Am Chem Soc*. 2019;141(16):6680-6689. https://doi.org/10.1021/jacs.9b01855
27. Zhao C, Li C, Yang Q, et al. Anionic redox reaction in Na-deficient layered oxide cathodes: role of Sn/Zr substituents

and in-depth local structural transformation revealed by solid-state NMR. *Energy Storage Mater*. 2021;39:60-69. https://doi.org/10.1016/j.ensm.2021.04.007
28. Hua W, Wang S, Knapp M, et al. Structural insights into the formation and voltage degradation of lithium- and manganese-rich layered oxides. *Nat Commun*. 2019;10(1):5365. https://doi.org/10.1038/s41467-019-13240-z
29. Yang L, Amo JML, Shadike Z, et al. A Co- and Ni-free P2/O3 biphasic lithium stabilized layered oxide for sodium-ion batteries and its cycling behavior. *Adv Funct Mater*. 2020;30(42):2003364. https://doi.org/10.1002/adfm.202003364
30. Gonzalo E, Zarrabeitia M, Drewett NE, López del Amo JM, Rojo T. Sodium manganese-rich layered oxides: potential candidates as positive electrode for sodium-ion batteries. *Energy Storage Mater*. 2021;34:682-707. https://doi.org/10.1016/j.ensm.2020.10.010
31. Cabana J, Chernova NA, Xiao J, et al. Study of the transition metal ordering in layered $Na_xNi_{x/2}Mn_{1-x/2}O_2$ ($2/3 \leq x \leq 1$) and consequences of Na/Li exchange. *Inorg Chem*. 2013;52(15):8540-8550. https://doi.org/10.1021/ic400579w
32. Bianchini M, Gonzalo E, Drewett NE, et al. Layered P2–O3 sodium-ion cathodes derived from earth abundant elements. *J Mater Chem A*. 2018;6(8):3552-3559. https://doi.org/10.1039/c7ta11180k
33. Zhang MJ, Teng G, Chen-Wiegart YK, et al. Cationic ordering coupled to reconstruction of basic building units during synthesis of high-Ni layered oxides. *J Am Chem Soc*. 2018;140(39):12484-12492. https://doi.org/10.1021/jacs.8b06150
34. Xiao B, Wang Y, Tan S, et al. Vacancy-enabled O3 phase stabilization for manganese-rich layered sodium cathodes. *Angew Chem Int Ed*. 2021;60(15):8258-8267. https://doi.org/10.1002/anie.202016334
35. Zuo W, Liu X, Qiu J, et al. Engineering Na^+-layer spacings to stabilize Mn-based layered cathodes for sodium-ion batteries. *Nat Commun*. 2021;12(1):4903. https://doi.org/10.1038/s41467-021-25074-9
36. Pei Y, Xu CY, Xiao YC, et al. Phase transition induced synthesis of layered/spinel heterostructure with enhanced electrochemical properties. *Adv Funct Mater*. 2017;27(7):1604349. https://doi.org/10.1002/adfm.201604349
37. Wu Z-G, Li J-T, Zhong Y-J, et al. Mn-based cathode with synergetic layered-tunnel hybrid structures and their enhanced electrochemical performance in sodium ion batteries. *ACS Appl Mater Interfaces*. 2017;9(25):21267-21275. https://doi.org/10.1021/acsami.7b04338
38. Xiao Y, Zhu YF, Xiang W, et al. Deciphering an abnormal layered-tunnel heterostructure induced by chemical substitution for the sodium oxide cathode. *Angew Chem Int Ed*. 2020;59(4):1491-1495. https://doi.org/10.1002/anie.201912101
39. Huang DQ, Wang DM, Zhang DL, et al. Shear-resistant interface of layered oxide cathodes for sodium ion batteries. *Energy Storage Mater*. 2021;45:389-398. https://doi.org/10.1016/j.ensm.2021.11.041
40. Shi Q, Qi R, Feng X, et al. Niobium-doped layered cathode material for high-power and low-temperature sodium-ion batteries. *Nat Commun*. 2022;13(1):3205. https://doi.org/10.1038/s41467-022-30942-z
41. Jin T, Wang PF, Wang QC, et al. Realizing complete solid-solution reaction in high sodium content P2-type cathode for high-performance sodium-ion batteries. *Angew Chem Int Ed*. 2020;59(34):14511-14516. https://doi.org/10.1002/anie.202003972
42. Wang PF, Yao HR, Liu XY, et al. Na^+/vacancy disordering promises high-rate Na-ion batteries. *Sci Adv*. 2018;4(3):eaar6018. https://doi.org/10.1126/sciadv.aar6018
43. House RA, Marie J-J, Pérez-Osorio MA, Rees GJ, Boivin E, Bruce PG. The role of O_2 in O-redox cathodes for Li-ion batteries. *Nat Energy*. 2021;6(8):781-789. https://doi.org/10.1038/s41560-021-00780-2
44. Li Q, Qiao Y, Guo S, et al. Both cationic and anionic Co-(de)intercalation into a metal-oxide material. *Joule*. 2018;2(6):1134-1145. https://doi.org/10.1016/j.joule.2018.03.010
45. Shi Y, Zhang Z, Jiang P, et al. Unlocking the potential of P3 structure for practical sodium-ion batteries by fabricating zero strain framework for Na^+ intercalation. *Energy Storage Mater*. 2021;37:354-362. https://doi.org/10.1016/j.ensm.2021.02.020
46. Rong X, Liu J, Hu E, et al. Structure-induced reversible anionic redox activity in Na layered oxide cathode. *Joule*. 2018;2(1):125-140. https://doi.org/10.1016/j.joule.2017.10.008
47. Zhang L, Wang J, Li J, et al. Preferential occupation of Na in P3-type layered cathode material for sodium ion batteries. *Nano Energy*. 2020;70:104535. https://doi.org/10.1016/j.nanoen.2020.104535
48. Zhang J, Kim J-B, Zhang J, et al. Regulating pseudo-Jahn–Teller effect and superstructure in layered cathode materials for reversible alkali-ion intercalation. *J Am Chem Soc*. 2022;144(17):7929-7938. https://doi.org/10.1021/jacs.2c02875
49. Paidi AK, Park WB, Ramakrishnan P, et al. Unravelling the nature of the intrinsic complex structure of binary-phase Na-layered oxides. *Adv Mater*. 2022;34(29):e2202137. https://doi.org/10.1002/adma.202270218
50. Rong X, Hu E, Lu Y, et al. Anionic redox reaction-induced high-capacity and low-strain cathode with suppressed phase transition. *Joule*. 2019;3(2):503-517. https://doi.org/10.1016/j.joule.2018.10.022
51. Liu Z, Shen J, Feng S, et al. Ultralow volume change of P2-type layered oxide cathode for Na-ion batteries with controlled phase transition by regulating distribution of Na^+. *Angew Chem Int Ed*. 2021;60(38):20960-20969. https://doi.org/10.1002/anie.202108109
52. Yu Y, Ning D, Li Q, et al. Revealing the anionic redox chemistry in O3-type layered oxide cathode for sodium-ion batteries. *Energy Storage Mater*. 2021;38:130-140. https://doi.org/10.1016/j.ensm.2021.03.004
53. Guo Y-J, Wang P-F, Niu Y-B, et al. Boron-doped sodium layered oxide for reversible oxygen redox reaction in Na-ion battery cathodes. *Nat Commun*. 2021;12(1):5267. https://doi.org/10.1038/s41467-021-25610-7
54. Liang X, Yu T-Y, Ryu H-H, Sun Y-K. Hierarchical O3/P2 heterostructured cathode materials for advanced sodium-ion batteries. *Energy Storage Mater*. 2022;47:515-525. https://doi.org/10.1016/j.ensm.2022.02.043
55. Yu Q, Tang W, Hu Y, et al. Novel low-cost, high-energy-density (>700 Wh kg^{-1}) Li-rich organic cathodes for Li-ion batteries. *Chem Eng J*. 2021;415:128509. https://doi.org/10.1016/j.cej.2021.128509
56. Kim CS, Guerfi A, Hovington P, et al. Facile dry synthesis of sulfur-$LiFePO_4$ core–shell composite for the scalable fabrication of lithium/sulfur batteries. *Electrochem Commun*. 2013;32:35-38. https://doi.org/10.1016/j.elecom.2013.03.037
57. Yi T-F, Li Y-M, Li X-Y, Pan J-J, Zhang Q, Zhu Y-R. Enhanced electrochemical property of $FePO_4$-coated $LiNi_{0.5}Mn_{1.5}O_4$ as cathode materials for Li-ion battery. *Sci Bull*. 2017;62(14):1004-1010. https://doi.org/10.1016/j.scib.2017.07.003
58. Liu C, Wang Z, Zong X, et al. N- & S-co-doped carbon nanofiber network embedded with ultrafine NiCo nanoalloy for efficient oxygen electrocatalysis and Zn–air batteries. *Nanoscale*. 2020;12(17):9581-9589. https://doi.org/10.1039/d0nr01516d
59. Azmi R, Trouillet V, Strafela M, Ulrich S, Ehrenberg H, Bruns M. Surface analytical approaches to reliably characterize lithium ion battery electrodes. *Surf Interface Anal*. 2018;50(1):43-51. https://doi.org/10.1002/sia.6330
60. Biesinger MC, Payne BP, Grosvenor AP, Lau LWM, Gerson AR, Smart RSC. Resolving surface chemical states in XPS analysis

of first row transition metals, oxides and hydroxides: Cr, Mn, Fe, Co and Ni. *Appl Surf Sci*. 2011;257(7):2717-2730. https://doi.org/10.1016/j.apsusc.2010.10.051

SUPPORTING INFORMATION

Additional supporting information can be found online in the Supporting Information section at the end of this article.

How to cite this article: Yang X, Wang S, Li H, et al. Unveiling the correlation between structural alterations and enhanced high-voltage cyclability in Na-deficient P3-type layered cathode materials via Li incorporation. *Electron*. 2024;2(1):e18. https://doi.org/10.1002/elt2.18